

## DEBRIS DISTRIBUTION IN HD 95086 – A YOUNG ANALOG OF HR 8799

KATE Y. L. SU<sup>1</sup>, SARAH MORRISON<sup>2</sup>, RENU MALHOTRA<sup>2</sup>, PAUL S. SMITH<sup>1</sup>, ZOLTAN BALOG<sup>3</sup>, GEORGE H. RIEKE<sup>1</sup>  
*accepted for publication in ApJ*

### ABSTRACT

HD 95086 is a young early-type star that hosts (1) a  $5 M_J$  planet at the projected distance of 56 AU revealed by direct imaging, and (2) a prominent debris disk. Here we report the detection of  $69 \mu\text{m}$  crystalline olivine feature from the disk using the *Spitzer*/MIPS-SED data covering 55–95  $\mu\text{m}$ . Due to the low resolution of MIPS-SED mode, this feature is not spectrally resolved, but is consistent with the emission from crystalline forsterite contributing  $\sim 5\%$  of the total dust mass. We also present detailed analysis of the disk SED and re-analysis of resolved images obtained by *Herschel*. Our results suggest that the debris structure around HD 95086 consists of a warm ( $\sim 175$  K) belt, a cold ( $\sim 55$  K) disk, and an extended disk halo (up to  $\sim 800$  AU), and is very similar to that of HR 8799. We compare the properties of the three debris components, and suggest that HD 95086 is a young analog of HR 8799. We further investigate and constrain single-planet, two-planet, three-planet and four-planet architectures that can account for the observed debris structure and are compatible with dynamical stability constraints. We find that equal-mass four-planet configurations of geometrically spaced orbits, with each planet of mass  $\sim 5 M_J$ , could maintain the gap between the warm and cold debris belts, and also be just marginally stable for timescales comparable to the age of the system.

*Subject headings:* circumstellar matter – infrared: stars, planetary systems – stars: individual (HD 95086)

### 1. INTRODUCTION

Hundreds of planetary systems have been discovered through radial velocity (Mayor et al. 2011) and transit measurements (Burke et al. 2014). However, this breakthrough is currently biased toward planetary architectures that may have experienced much more dynamical evolution and reflect conditions that are different from our own Solar System. Probing planets similar to our own Solar System (giant planets located outside 5 AU with orbital periods longer than 10 years) requires either long-term monitoring or advanced instruments that can significantly reduce the light from the host stars, which are both technically challenging. Debris disks offer an indirect way to study outer planetary systems. Debris disks are tenuous dusty structures sustained through collisions of leftover planetesimals and minor bodies such as asteroids, Kuiper Belt Objects (KBOs) and comets (often referred as parent bodies), that failed to form planets. The loss timescale for dust in a typical debris system is generally less than  $10^4$  years; therefore, the presence of dust around a main-sequence star requires a replenishing reservoir and one or more large bodies providing dynamical stirring to maintain a high rate of collisions among the debris parent-body reservoir. The large surface area of debris makes these disks detectable through infrared and millimeter thermal emission or optical scattered light, providing insights into the nature of unseen parent-body populations and massive planetary perturbers. Because debris disks are detected from just after the protoplanetary stage to nearly the end of the star’s life billions of

years later, they are excellent observational tools to study the growth of planets and subsequent dramatic steps that determine the architecture of planetary systems.

In our Solar System, the stable locations of the left-over planetesimals (i.e., the asteroid and Kuiper belts) are tightly coupled with the architecture of the planets. In an analogous fashion, the observed debris structures around other stars such as the tilted inner disk in  $\beta$  Pic (Heap et al. 2000; Golimowski et al. 2006) and the eccentric ring in Fomalhaut (Stapelfeldt et al. 2004; Kalas et al. 2005) have long been used to predict the presence of unseen planets. This connection became even more persuasive when the first few directly imaged planets were discovered around debris-host stars (HR 8799: Marois et al. 2008, Fomalhaut: Kalas et al. 2008, and  $\beta$  Pic: Lagrange et al. 2009). In addition, some debris systems are known to possess dust emission at two different temperatures, suggesting a cold outer belt accompanied by a fainter, warm inner one (e.g., Chen et al. 2009; Morales et al. 2011; Ballering et al. 2013; Kennedy & Wyatt 2014). Although there might be many mechanisms to explain such a large gap, a probable way to maintain this structure is shown by the four super-Jupiter-like planets around HR 8799 (Marois et al. 2010), which are packed between inner and outer debris disk components as revealed by resolved imaging and detailed analysis of the spectral energy distribution (SED) (Su et al. 2009). The similar large gaps between the inner and outer debris components around other stars may be maintained by lower-mass planets; for example, in the debris disk twins (Vega and Fomalhaut), we have strong evidence that the large gap between the warm asteroid-like and the cold KBO-like dust belts is an excellent signpost for multiple ice-giant-mass planets beyond the ice line (Su et al. 2013). A large gap of this type between the inner warm and outer cold belts is an example of a

<sup>1</sup> Steward Observatory, University of Arizona, 933 N Cherry Ave., Tucson, AZ 85721; ksu@as.arizona.edu

<sup>2</sup> Lunar and Planetary Laboratory, University of Arizona, Tucson, AZ 85721, USA

<sup>3</sup> Max-Planck-Institut für Astronomie, Königstuhl 17 D-69117, Heidelberg, Germany

global disk feature that points toward general aspects of planetary system formation and evolution.

The SEDs of debris disks can be understood, to first order, by assuming that there are various zones that are maintained by common factors, e.g., fossil ice lines and ice giant planets. The diversity of disk structures and SEDs then reflect variations in the amount of material in these zones, that are closely related to different paths by which a system forms and evolves, rather than radical differences in structure (Su & Rieke 2014). Hence, systems that harbor directly-imaged planets and debris disks are valuable tools to better understand planetary system formation and evolution.

In this study, we focus on the planetary system around HD 95086. The star is an early-type member of the Lower Centaurus Crux Association (LCC; de Zeeuw et al. 1999; Rizzuto et al. 2012), and located  $90.4 \pm 3.4$  pc away (van Leeuwen 2007). The age of the star has been reviewed by Meshkat et al. (2013) with an estimate of 17 Myr ( $\pm 2$  Myr statistical and  $\pm 4$  Myr systematic). HD 95086 has drawn a lot of attention lately because it hosts a directly imaged planet HD 95086b at a projected distance of 56 AU (Rameau et al. 2013a). The planet has very red infrared colors, similar to young massive planets HR 8799 bcde and 2M 1207b, with a mass estimate of  $5 \pm 2 M_J$  based on evolutionary models (Meshkat et al. 2013; Rameau et al. 2013b; Galicher et al. 2014). HD 95086 also has a prominent infrared excess with a dust fractional luminosity ( $f_d$ ) of  $1.6 \times 10^{-3}$  (Rhee et al. 2007; Chen et al. 2012). The debris around HD 95086 was marginally resolved at far-infrared wavelengths with *Herschel*, suggesting a slightly inclined orientation from face-on (Moór et al. 2013). There are some inconsistencies in the disk properties of HD 95086 in the literature. We, therefore, review existing infrared photometric and spectroscopic data, and present an unpublished *Spitzer* MIPS-SED low-resolution spectrum covering 55–95  $\mu\text{m}$  for a comprehensive disk SED analysis (Section 2). To thoroughly exploit the opportunity that the HD 95086 system provides, we also re-analyze the *Herschel* resolved images in comparison with the SED modeling results, and conclude that the resolved debris structure is mostly in the form of a disk halo composed of small grains (Section 3). In Section 4, we discuss the similarity between HD 95086 and HR 8799 in their debris distribution, and provide dynamical constraints on possible planetary configurations in HD 95086. Our conclusions are presented in Section 5.

## 2. OBSERVATIONS AND DATA REDUCTION

We present unpublished *Spitzer* MIPS-SED data and review all published infrared/submillimeter observations for the HD 95086 system. Our goal is to construct a detailed disk SED that can be used to estimate the location of debris within the system.

### 2.1. Infrared/Submillimeter Broad-Band Photometry

*Spitzer* MIPS photometry was first published by Chen et al. (2012) where fluxes were extracted using Point Spread Function (PSF) fitting designed for point sources. We examined the 24  $\mu\text{m}$  image, and found the source is slightly extended (Full-Width-Half-Maximum (FWHM) of  $5''.98 \times 5''.87$ , compared to a typical point

source’s FWHM  $5''.49 \pm 0''.03 \times 5''.45 \pm 0''.03$ ). Therefore, we adopted measurements with photometry through a large aperture (aperture radius of  $14''.9$  and sky annulus of  $29''.9 - 42''.3$ ), resulting in  $52.95 \pm 0.55$  mJy as the total 24  $\mu\text{m}$  flux for the system ( $\sim 16\%$  higher than the PSF extracted flux). At 70  $\mu\text{m}$ , the source is point-like with a total flux of  $655 \pm 33$  mJy. The quoted flux uncertainties include instrumental repeatability, which is 1% and 5% at 24 and 70  $\mu\text{m}$ , respectively.

*Herschel* PACS and SPIRE observations were first published by Moór et al. (2013), and showed that the disk was resolved at 70 and 100  $\mu\text{m}$  with an estimated inclination angle of  $25^\circ$ . Because the *Herschel* observations were reduced with an older pipeline (HIPE v9.2), we re-reduced the data with an updated pipeline (HIPE v13.0) that incorporated many new calibration improvements detailed in Balog et al. (2014). Specifically, we included the experimental tool for pointing reconstruction based on the gyroscope information that considerably reduces the pointing jitter and increases the stability of the PSF (termed as gyro correction). Finally, we mosaicked the final maps with a default “pixfrac” parameter 1.0, equivalent to drizzle parameter of 0.8, in the instrumental orientation so the PSF structures were always in the same location. No rotation/interpolation is then needed in further PSF subtraction analyses. Detailed analysis of the PACS images is presented in Section 3.1. We used an aperture size of  $22''$  at all three bands to measure the source flux, at which radius the encircled flux reached the maximum and flattened afterward (after proper aperture correction). We did not apply color correction for the PACS fluxes. The final PACS fluxes are:  $688 \pm 48$ ,  $688 \pm 48$ , and  $489 \pm 35$  mJy at 70, 100, and 160  $\mu\text{m}$ , respectively, in good agreement with the Moór et al. (2013) published results.

Inspecting the SPIRE maps, the source is clearly detected at all three wavelengths as a point source, and the surrounding field has no bright source or large-scale extended structure. Therefore, we used the level 2 point-source product (Jy/beam) provided by the Herschel Science Center (HIPE ver. 11) to measure fluxes. We used the peak value of the source to estimate the point-source flux. After correcting the pixelisation effect (0.951, 0.931, 0.902 at 250, 350, and 500  $\mu\text{m}$ , respectively; SPIRE Handbook, version 2.5, 2014), the source submillimeter fluxes are:  $186 \pm 16$  mJy,  $112 \pm 16$  mJy, and  $67 \pm 17$  mJy at 250, 350, and 500  $\mu\text{m}$ , respectively. At 500  $\mu\text{m}$ , there are a couple of faint peaks within  $40''$  of the target, which might contaminate the submillimeter fluxes. No color correction was applied for the SPIRE fluxes either. Our SPIRE fluxes are lower than the values published by Moór et al. (2013) who extracted source fluxes using aperture photometry, but consistent within uncertainties. Finally, HD 95086 was detected at 870  $\mu\text{m}$  with the submillimeter telescope APEX by Nilsson et al. (2010). Its nominal beam size is  $19''.2$  (FWHM), but the effective resolution is  $27''$  after filtering and smoothing in the data reduction (Nilsson et al. 2010). The source at 870  $\mu\text{m}$  appears to be elongated (Figure 2 in Nilsson et al. 2010) and surrounded by faint peaks. Therefore, it is likely that the measured 870  $\mu\text{m}$  flux ( $41.3 \pm 18.4$  mJy) is over-estimated and contaminated by background galaxies.

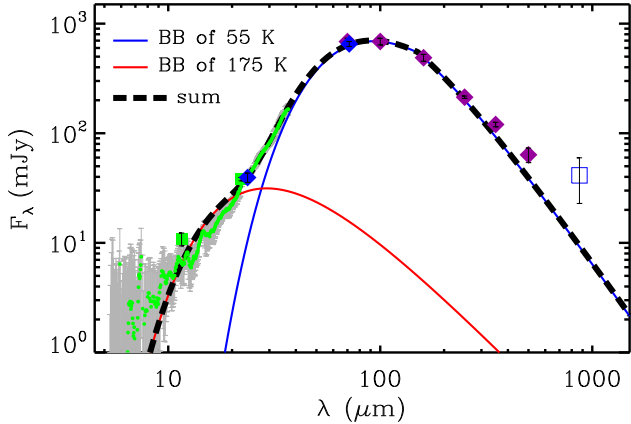


FIG. 1.— The excess SED of the HD 95086 system composed of broad-band photometry and the mid-infrared spectrum after subtraction of the stellar contribution. The excess flux uncertainty ( $1\sigma$ ) includes 2% of the photospheric emission added quadratically. The broad-band fluxes include: blue diamonds from *Spitzer*, purple diamonds from *Herschel*, green squares from *WISE* and a blue open square from APEX/870 observation (Nilsson et al. 2010).

## 2.2. Spectroscopy – *Spitzer* IRS and MIPS-SED

A *Spitzer* IRS spectrum of the system was first published by Chen et al. (2006) where the excess spectrum was characterized by blackbody emission of  $80 \pm 30$  K. The same spectrum was reduced and analyzed by Moór et al. (2013), who found the spectral shape of the excess along with long-wavelength photometry is better fitted with two blackbody temperatures:  $187 \pm 26$  K and  $57 \pm 1.5$  K. Finally, Chen et al. (2014) characterized the excess to be consistent with two temperatures:  $225_{-7}^{+10}$  K and  $57 \pm 5$  K. The warm temperature discrepancy might be due to how the two IRS modules were joined and scaled relative to the photosphere. For this reason, we also performed the IRS data reduction, similar to what was done in Moór et al. (2013) but with the SMART software (ver. 8.2.7; Higdon et al. 2004). The two low resolution modules (short-low (SL):  $5.2\text{--}14.5 \mu\text{m}$  and long-low (LL):  $14.0\text{--}38.0 \mu\text{m}$ ) were extracted and combined independently using SMART’s optimal 2 nod extraction (Lebouteiller et al. 2010). The SL spectrum agrees very well ( $<1\%$ ) with the expected Kurucz model flux for wavelengths shorter than  $6.5 \mu\text{m}$ , while the LL spectrum was scaled down (by 0.963) to match the MIPS  $24 \mu\text{m}$  large aperture photometry. The two modules then joined smoothly without further scaling.

The photospheric contribution was subtracted using the best-fit Kurucz model ( $T_{\text{eff}} = 7500\text{K}$  and  $\log g = 4.0$ ), and 2% of the photospheric emission was included in computing the excess flux uncertainty. Figure 1 shows the excess SED composed of broad-band photometry and the IRS spectrum. Our best-fit (weighted by the uncertainty) two blackbody temperatures are  $55 \pm 5$  K (cold component) and  $175 \pm 25$  K (warm component). The large error in the warm temperature is driven by the large uncertainty in the  $7\text{--}10 \mu\text{m}$  excess flux after photospheric subtraction. The 175 K blackbody emission slightly (within  $1\sigma$ ) under predicts the excess flux shortward of  $10 \mu\text{m}$ , suggesting either the system has another faint, hotter component or the emission from the warm component has a weak silicate feature from  $\sim \mu\text{m}$ -size grains. We have used the fitting technique developed by

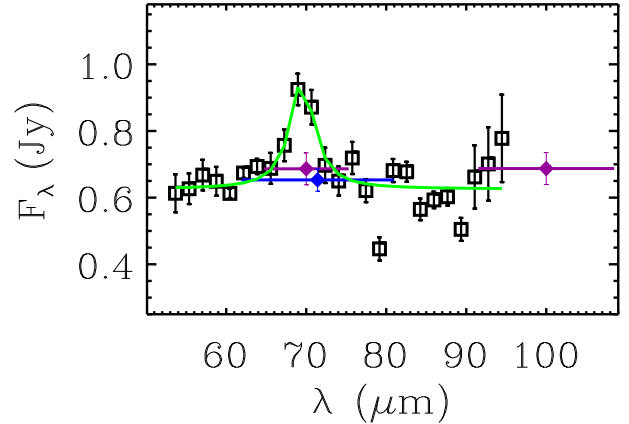


FIG. 2.— The panel shows the excess MIPS-SED spectrum (black squares). A crystalline olivine feature is detected where a Lorentzian profile fit (green line) suggests the feature peaks at  $69.5 \pm 0.5 \mu\text{m}$  and is not spectrally resolved. The MIPS-SED spectrum agrees well with the broad-band photometry (diamonds).

Ballerling et al. (2014), including various normalizations of the photosphere, to evaluate this emission. We find no evidence for silicate emission features, thus differing from those excesses identified by Ballerling et al. (2014); instead, within the errors, a  $\sim 300$  K blackbody is an adequate fit. Adding this component has negligible effect on the fitted temperature of the 175 K component (reducing its temperature by about 10 K). Given its large uncertainty, we do not include this tentative, faint and hotter component in our following discussion.

The MIPS-SED data were obtained in 2006 Feb 20 (AOR key 16171264, PID 84, PI: Jura) with the  $10 \text{ s} \times 10 \text{ cycles}$  and  $1'$  chop setting, resulting in a low-resolution ( $R = 15\text{--}25$ ) spectrum from  $55$  to  $95 \mu\text{m}$  with 600 s of integration on source. The data were reduced and calibrated as described by Lu et al. (2008). An extraction aperture of  $50''$  in the spatial direction was used, and the slit loss was corrected assuming a point source. We trimmed off the spectrum past  $95 \mu\text{m}$  because of known contamination by the blue end of the second-order spectrum produced in this observing mode of the instrument that cannot be calibrated (Lu et al. 2008). The photosphere-subtracted MIPS-SED spectrum is shown in Figure 2, where a feature peaking near  $\sim 70 \mu\text{m}$  can be seen. There is also one low discrepant point near  $80 \mu\text{m}$  (by  $2\text{--}3\sigma$ ) that is problematic. We investigated the discrepancy and were not able to find an obvious reason outside the possible transient systematic errors in the array around  $80 \mu\text{m}$ . However, the feature at  $\sim 70 \mu\text{m}$  appears to be real since it consists of two high points that are  $\gtrsim 3\sigma$  above the overall continuum, and several adjacent points that are consistent with the instrumental resolution, unlike the single low point at  $80 \mu\text{m}$ . We have also checked other MIPS-SED spectra for sources that have similar  $70 \mu\text{m}$  fluxes as HD 95086, and none were found to have such an emission feature, suggesting that it is not due to instrumental artifacts. The shape of the MIPS-SED spectrum is consistent with the broad-band photometry measured by PACS and MIPS at  $70 \mu\text{m}$ . Since the bandwidth of the MIPS  $70 \mu\text{m}$  filter is wider than that of the PACS  $70 \mu\text{m}$  filter, the slightly lower value of the MIPS  $70 \mu\text{m}$  measurement is consistent with the presence of the expected feature. A Lorentzian profile fit to

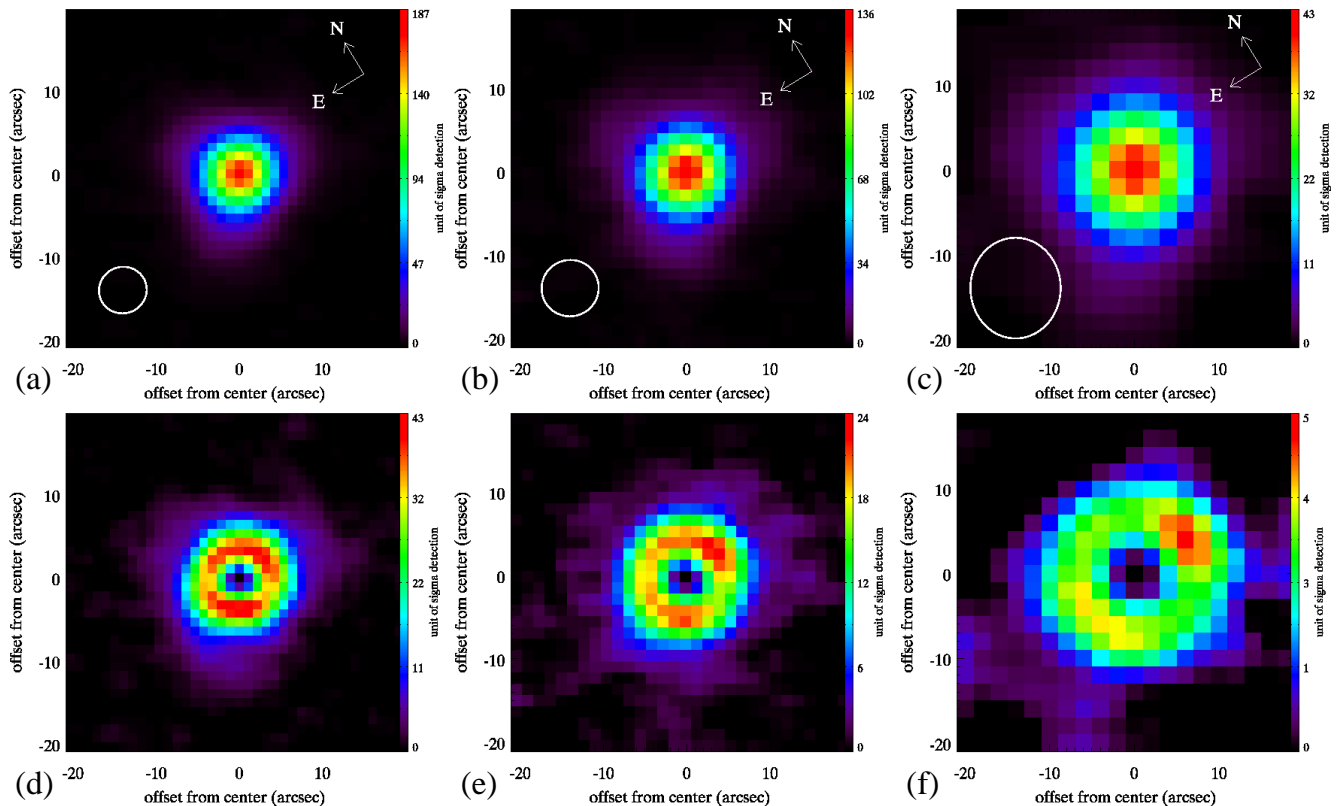


FIG. 3.— *Herschel* PACS images of HD 95086. The upper row shows PACS images at (a) 70  $\mu\text{m}$ , (b) 100  $\mu\text{m}$ , and (c) 160  $\mu\text{m}$ , respectively. The bottom row shows the PSF-subtracted (normalized to the peak of the source) residual images at (d) 70  $\mu\text{m}$ , (e) 100  $\mu\text{m}$ , and (f) 160  $\mu\text{m}$ , respectively. The beam sizes are shown as white ellipses in the upper panels.

the MIPS-SED spectrum suggests that the feature peaks at  $69.5 \pm 0.5 \mu\text{m}$  with a linewidth (FWHM) of  $4.2 \mu\text{m}$ , consistent with an emission-line feature that is not spectrally resolved in the MIPS-SED mode. Given the cold dust temperature ( $55 \pm 5 \text{ K}$ ), the measured peak position is consistent with the laboratory measurement of crystalline olivine ( $\text{Mg}_2\text{SiO}_4$ , forsterite) at 50 K (Suto et al. 2006). The 69  $\mu\text{m}$  band strength (integrated luminosity) is  $8.3 \times 10^{-13} \text{ erg cm}^{-2} \text{ s}^{-1}$ , which is in the range of detected band strengths around protoplanetary disks (see Table 2 in Maaskant et al. 2014). This feature has also been detected in the  $\beta$  Pic debris disk using the *Herschel* PACS spectrometer (de Vries et al. 2012). We discuss the possible implications of the presence of the 69  $\mu\text{m}$  feature in Section 4.2.

### 3. ANALYSIS

#### 3.1. PACS Imaging Analysis

Fully understanding the instrumental PSFs is essential in characterizing resolved images; especially it has been shown that the high-pass filtering and drizzling methods for coadding images used in HIPE have a great impact on the resultant PSF and noise characteristics (Popesso et al. 2012). We, therefore, carried out some basic PACS PSF characterization by using PACS data for  $\gamma$  Dra, a routine calibrator, that were observed throughout *Herschel*'s operation. We used the data obtained in the mini-scan map mode with two scan angles of  $70^\circ$  and  $110^\circ$  only (the same as the HD 95086 data). These data were processed with the same pipeline and procedure as our target star (same filtering width, masking radius, pixfrac, instrumental orientation and gyro cor-

rection). We further inspected the quality of the data by measuring the FWHM of each observation and rejected data sets that have deviant values. Finally, we obtained a high signal-to-noise, co-added  $\gamma$  Dra image by median combining sets of 26, 5 and 26 observations at 70, 100 and 160  $\mu\text{m}$ , respectively. These combined, high-quality  $\gamma$  Dra data were used as our point source standards when assessing the resolvability of an observation.

All the FWHM measurements were measured by fitting a 2-D Gaussian function on sub-regions centered at the target with fields of view (f.o.v.) of  $21''.1$ ,  $29''.4$ , and  $44''.1$  at 70, 100 and 160  $\mu\text{m}$ , respectively. Note that different values of f.o.v. would result in slightly different FWHM values; therefore, it is important to be consistent with the f.o.v. used in comparisons. The average FWHMs for the  $\gamma$  Dra data are:  $5''.75 \pm 0''.08 \times 5''.56 \pm 0''.04$  with Position Angle (P.A.) of  $32^\circ \pm 29^\circ$  at 70  $\mu\text{m}$ ,  $6''.85 \pm 0''.04 \times 6''.70 \pm 0''.04$  with P.A. of  $33^\circ \pm 26^\circ$  at 100  $\mu\text{m}$ , and  $11''.97 \pm 0''.16 \times 10''.69 \pm 0''.15$  with P.A. of  $91^\circ \pm 5^\circ$  at 160  $\mu\text{m}$ . The beam (defined as the FWHM) is more elongated in the 160  $\mu\text{m}$  channel and with a preferred P.A. compared with the beams at 70 and 100  $\mu\text{m}$ . The variations in the measured FWHMs are all less than 2%, demonstrating the effectiveness of the new gyro correction.

The final PACS images are shown in the upper panel of Figure 3. The measured FWHMs for the HD 95086 PACS data are:  $7''.87 \times 7''.47$  with P.A. of  $112^\circ$  at 70  $\mu\text{m}$ ,  $8''.91 \times 8''.43$  with P.A. of  $116^\circ$  at 100  $\mu\text{m}$ , and  $13''.4 \times 12''.2$  with P.A. of  $140^\circ$  at 160  $\mu\text{m}$ , suggesting the source is resolved at  $\sim 1.4$  beams at both 70/100  $\mu\text{m}$ , but only at  $\sim 1.1$  beams at 160  $\mu\text{m}$ . This explains why the P.A.

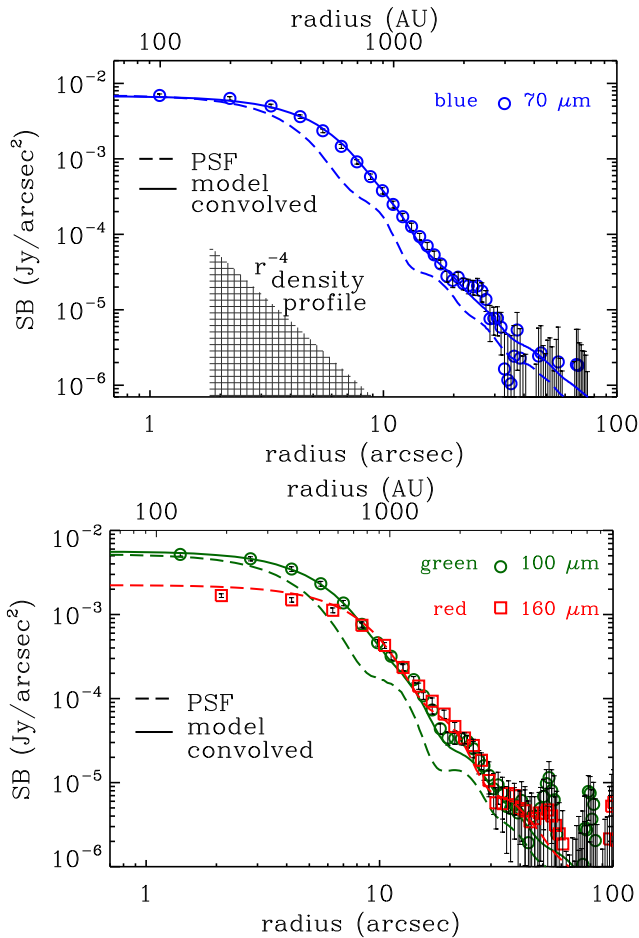


FIG. 4.— The azimuthally averaged radial surface brightness (SB) profiles for HD 95086 (open circles: blue for data at  $70\ \mu\text{m}$ , green for data at  $100\ \mu\text{m}$ , and red for data at  $160\ \mu\text{m}$ ). The stellar contribution is negligible in the far-infrared. The radial profile of  $\gamma$  Dra (point source calibrator) is shown in dashed lines. Solid lines show the best-fit single power-law SB model after being convolved with the PSF while the hash region on the upper panel illustrates the model parameters ( $\alpha = 4$ ,  $r_{in} = 1''.8$ , and  $r_{out} = 9''$ ; details see the text).

measured at  $160\ \mu\text{m}$  is quite different from the ones at  $70/100\ \mu\text{m}$ . Based on the resolvability ( $\lesssim 1.4$  beam), we simulated model images at all three bands (for details see below) and at different inclinations, compared with the derived FWHMs and aspect ratio, and concluded that the source is inclined at  $25^\circ \pm 5^\circ$  at P.A. of  $115^\circ \pm 10^\circ$ . These values agree with the numbers derived by Moór et al. (2013).

The source is resolved at  $\lesssim 1.4$  beams, consistent with the observation that the images at all three wavelengths are centrally peaked. To estimate the maximum flux of a point source in the data, we performed PSF subtraction using the  $\gamma$  Dra combined PSF by matching the peak value at the center. The PSF-subtracted images are shown in Figure 3 bottom row. The scaled point source fluxes are 397 mJy, 422 mJy, and 357 mJy at  $70$ ,  $100$ , and  $160\ \mu\text{m}$ , respectively, which are  $\sim 262$ ,  $\sim 574$ , and  $\sim 1266$  times the expected photospheric values at these wavelengths. The scaled point source fluxes are also much brighter than the expected values of the warm component ( $< 10$  mJy, see Figure 1). It is clear that a significant amount of dust emission (presumably from a

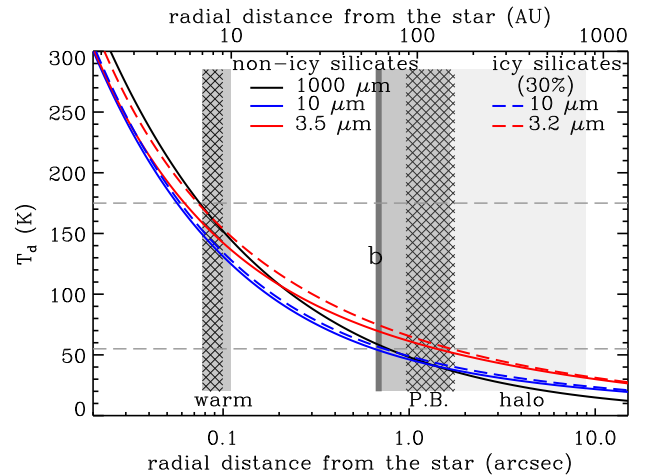


FIG. 5.— The dust temperature distribution for both astronomical silicates and icy silicates at selected grain sizes. The two horizontal dashed lines mark the two observed dust temperatures from the disk SED. The location of the HD 95086b is marked at 62 AU. The ranges of the flat disk models are marked as dark gray areas while the ones of Gaussian ring models are marked as hashed areas for both the warm belt and cold planetesimal belt (P.B.). The light gray area shows the range of the disk halo.

planetesimal belt, P.B.) is not resolved (up to  $\sim 58\%$ ,  $\sim 61\%$ , and  $\sim 73\%$  at  $70$ ,  $100$ , and  $160\ \mu\text{m}$ , respectively); i.e.,  $\gtrsim 30\text{--}40\%$  of the total excess fluxes is in the resolved structure.

We adopted a similar strategy as in Su et al. (2009) and Matthews et al. (2014) to investigate simple structural parameters that would be consistent with the resolved images. The model images were constructed for a given model description, projected to the inclination angle of  $25^\circ$ , then convolved with the appropriate PSF. We then computed the azimuthally averaged radial profiles for both the observed and model data for comparison. Since PACS  $70\ \mu\text{m}$  and  $100\ \mu\text{m}$  channels have the better resolutions, we derived the best-fit parameters only for the  $70/100\ \mu\text{m}$  data, and verified them with the  $160\ \mu\text{m}$  data. The model surface brightness (SB) was normalized to the observed profile for data points within  $7''$  (ensuring good fits in the high signal-to-noise region), then we computed the  $\chi^2$  values for data points within  $20''$  at  $70\ \mu\text{m}$ , and  $15''$  at  $100\ \mu\text{m}$ , respectively. Limited by the marginally resolved images, we only explored a simple power-law distribution ( $SB(r) \sim r^{-\alpha}$ ) with inner ( $r_{in}$ ) and outer ( $r_{out}$ ) radial cutoffs. With  $\alpha = 3$ , we found  $r_{in} \sim 1''.3$  and  $r_{out} \sim 9''$ . With  $\alpha = 4$ , we found  $r_{in} \sim 1''.8$  and  $r_{out} \sim 9''$ . Alternatively, we could also find reasonable fits for the case of  $\alpha = 1$ , which is the power index for the planetesimal belt derived for the resolved images of HR 8799 (Matthews et al. 2014). In summary, the power-law index ( $\alpha$ ) is unconstrained, and the resolved images are best described as a point source plus some form of extended structure. As we discuss in Section 3.2, the resolved structure in the HD 95086 system most likely arises from the disk halo component composed of only small grains that can be warm enough to emit efficiently at far-infrared wavelengths to account for the extended structure seen in the PACS images. We note that the disk halo component is found to have  $\alpha = 3\text{--}4$  for HR 8799 (Matthews et al. 2014). With this assumption, the derived  $r_{in}$  ( $\sim 120\text{--}165$  AU) represents the boundary where the halo emission becomes dominant (i.e., the outer ra-

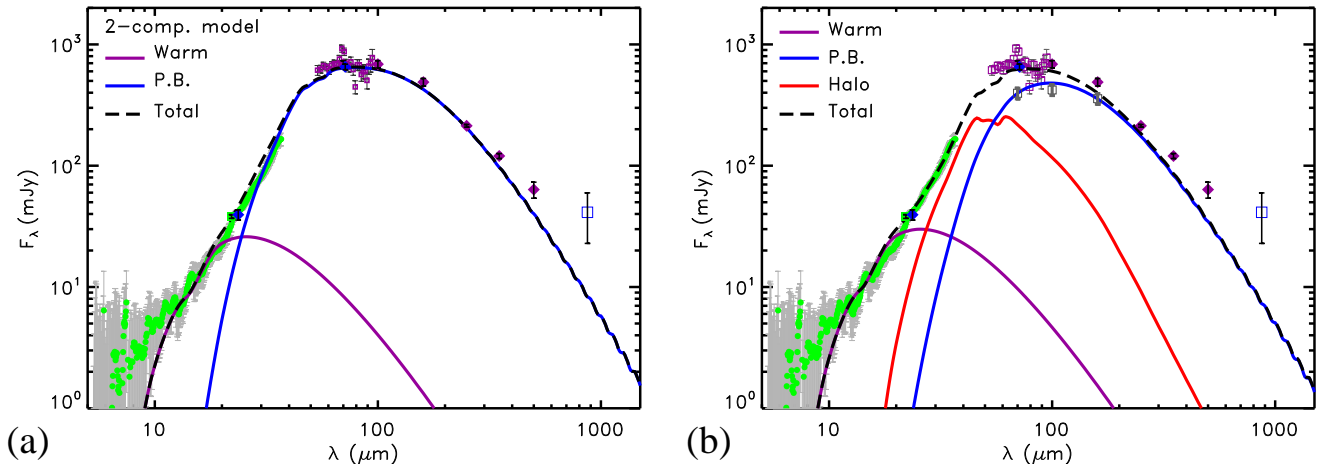


FIG. 6.— The spectral energy distribution (SED) of the debris around HD 95086. In both panels, various points show the infrared excesses after the removal of the stellar photosphere (symbols are used the same way as in Figure 1), except that MIPS-SED data are shown as purple squares with grey error bars. Panel (a) shows the SEDs for the two-component model. The infrared excesses can be described with two separated flat disks: warm disk (purple thick line:  $R_{in} = 7$  AU and  $R_{out} = 10$  AU) and planetesimal disk (thick blue line:  $R_{in} = 63$  AU and  $R_{out} = 189$  AU). Panel (b) shows one of the possible three-component models that provide a good fit to the overall SED and resolved images. Symbols used are the same as panel (a) except for the new open squares representing the maximum fluxes of the planetesimal belt at the PACS wavelengths (details see the end of Section 3.2).

dius of the planetesimal belt), while the  $r_{out}$  ( $\sim 800$  AU) only represents the boundary where the faint disk halo can be well detected given the sensitivity. The best-fit SB distributions are shown in Figure 4 along with the observed profiles. Unlike the HR 8799 SB profiles where two power-laws were required to fit the data, one single power-law model provides satisfactory fits to the HD 95086 data.

### 3.2. SED modeling and Derived Parameters

To guide the SED modeling, we first computed the thermal equilibrium dust temperature distribution around HD 95086 (Figure 5) with assumed grain properties in an optically thin environment. We adopted two grain compositions: astronomical silicates and ice-coated silicates. We used the optical constants from Laor & Draine (1993) and Mie theory code to compute the grain absorption and scattering efficiency for compact, spherical astronomical silicates. For the absorption and scattering efficiency of icy grains, we used both multi-layer Mie calculations as well as standard effective medium theory rules (Garrett and Bruggeman equation) (e.g., Voshchinnikov et al. 2005). For the inner warm belt, we adopt compact astronomical silicates as the composition for the SED fitting since the majority of the ice should be sublimated at the warm belt temperature. For the outer cold disk, we use the icy grains composed of compact silicate cores with icy mantles that occupy 30% of the grain volume. The thickness of the icy mantles is chosen so that the resultant model emission produces a good overall fit in the 60–70  $\mu\text{m}$  region. Figure 5 shows that in terms of these two grain compositions (non-icy vs. icy) the resultant temperatures for grains larger than  $\sim 10 \mu\text{m}$  are not very different, but they could have  $\gtrsim 10$  K difference for  $\mu\text{m}$ -size grains closer in. The observed two characteristic temperatures ( $\sim 175$  K and  $\sim 55$  K) suggest two distinct dust locations ( $\sim 7$  AU and  $\sim 60$  AU) for blackbody-like grains.

Since fine debris is generated through collisional cascades by breaking up large parent bodies, we expect

a full spectrum of particle sizes in a debris disk, generally in a power-law form,  $n(a) \sim a^{-q}$  with  $n$  being the number density,  $a$  for the grain radius and  $q = 3.5\text{--}3.7$  (Wyatt et al. 2011; Gáspár et al. 2012). Thus, the majority of particles in a collisional dominated disk are grains just slightly larger than the minimum grain size in the distribution (i.e., the average grain size is  $\langle a \rangle \sim \frac{q-1}{q-2} a_{min}$  where  $a_{min}$  is the minimum size of grains existing in a steady-state collisional disk). In a debris disk (no/very little gas), in addition to the gravitational force of the star, dust grains are subject to radiation pressure. Therefore, grains that are smaller than the blowout size ( $a_{bl}$ ) are removed from the system, i.e.,  $a_{min} \sim a_{bl}$ . The blowout size is a function of stellar mass ( $M_*$ ), luminosity ( $L_*$ ) and grain density ( $\rho$ ) given by  $a_{bl} = 1.15 \frac{L_*}{L_\odot} \frac{M_\odot}{M_*} \frac{g/cm^3}{\rho}$  in units of  $\mu\text{m}$ . Given the stellar parameters for HD 95086 ( $L_* \sim 7 L_\odot$  and  $M_* \sim 1.6 M_\odot$ ), the radiation blowout radius is 1.5 and 1.8  $\mu\text{m}$  for densities of  $3.3 g/cm^3$  (for compact silicates) and  $2.6 g/cm^3$  (for icy silicates), respectively. Therefore, the average grain sizes in such a collisionally dominated disk are  $\sim 3 \mu\text{m}$ . We also set the maximum grain radius ( $a_{max}$ ) to be 1000  $\mu\text{m}$ ; grains larger than this size have negligible contribution to the model emission.

In our simple SED model, we adopt a uniform particle size distribution at all astro-centric distances and do not consider the effect of grain size segregation due to stellar radiation pressure. The grain-size segregation in debris disks is closely tied to the complex coupling between dynamical and collisional effects (e.g., Thebault et al. 2014); therefore, the impact of using a uniform size distribution is difficult to evaluate without multi-wavelength resolved images. For simplicity, we adopt  $q = 3.5$  for the cold disk component because the cold disk, as we show later, is quite extended ( $\sim 63\text{--}190$  AU), and the particle distribution for a unperturbed wide disk is most likely to have  $q = 3.5$  distribution based on the computation of Thebault et al. (2014). For the inner warm component, on the other hand, we adopt a steeper power

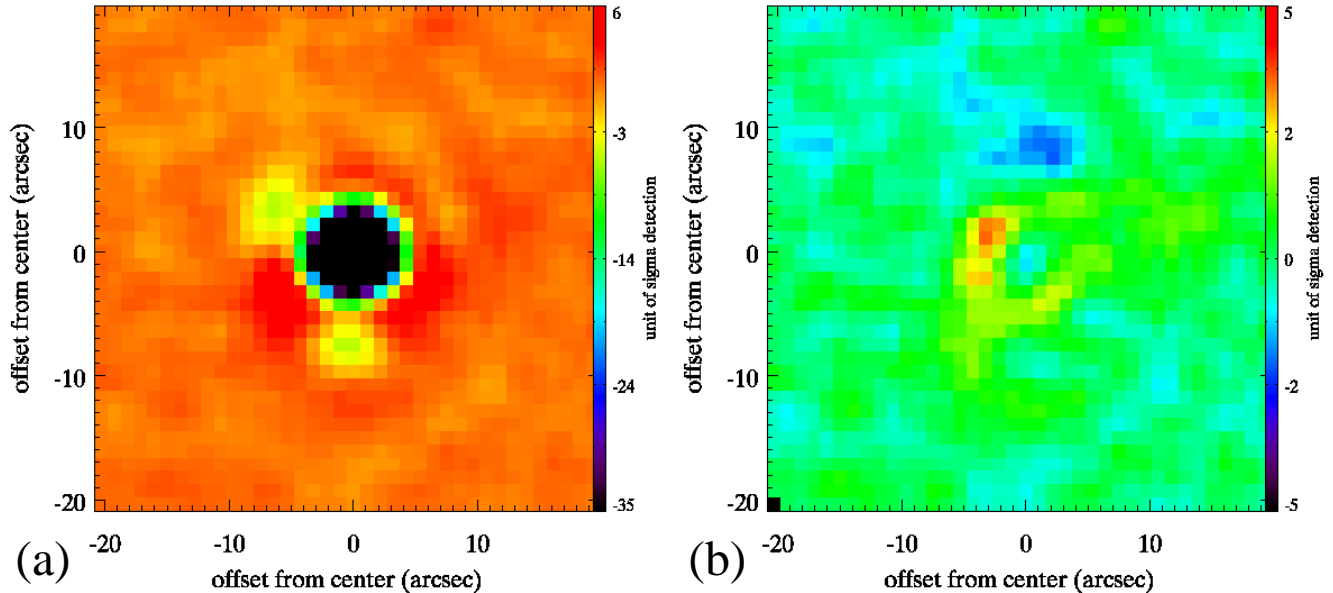


FIG. 7.— Difference images at  $70\ \mu\text{m}$  between observed and model images: panel (a) using the two-component model while panel (b) using the three-component model. The over-subtraction (more than  $-100\sigma$  at the center) in (a) is due to the fact that the two-component model has no disk contribution outside the typical beam (i.e., not resolved). In the three-component model, some portion of the disk flux is distributed outside the beam (i.e., resolved disk halo), and the residuals for the three-component model are within  $\pm 2\sigma$ .

law,  $q = 3.65$ , based on the hypothesis that the warm component is a narrow belt closer to the star where collisional cascades are expected to reach collisional equilibrium (Gáspár et al. 2012; Thebault et al. 2014). Although the output far-infrared and submillimeter fluxes would be slightly different depending on the  $q$  values, the adopted  $q$  value has little impact on our model parameters for the warm component since we have no far-infrared/submillimeter constraint.

Two kinds of simple density distributions were used to construct the disk SED. One is a flat disk (constant surface density) with adjustable inner ( $R_{in}$ ) and outer ( $R_{out}$ ) radii, and the other one is a Gaussian profile ring with a peak radius ( $R_p$ ) and a width ( $R_w$  as the FWHM). With the grain parameters (composition and size distribution) set, we searched for the best-fit two parameters in each density distribution. Because the warm and cold components are not spatially resolved and the (expected) peak emission of the warm component (see Figure 1) is in the region where emission from the cold component also contributes significantly, our SED fitting strategy is to obtain reasonable fits to the cold component first, then derive parameters for the warm component. For the cold component, we only used the data points longward of  $35\ \mu\text{m}$  and shortward of  $500\ \mu\text{m}$  to derive the best-fit (in  $\chi^2$  sense) size parameters. In the flat disk model, the best-fit disk extension is:  $R_{in} = 63 \pm 6\ \text{AU}$  and  $R_{out} = 189 \pm 13\ \text{AU}$ ; while the Gaussian ring model gives  $R_p = 123 \pm 3\ \text{AU}$  with a width of  $R_w = 72 \pm 11\ \text{AU}$ . For the cold disk, the derived dust fractional luminosity is  $\sim 1.5 \times 10^{-3}$  with dust mass (up to  $1000\ \mu\text{m}$ ) of  $0.18 \pm 0.01 M_{\oplus}$  for the flat disk, and  $0.23 \pm 0.01 M_{\oplus}$  for the Gaussian ring model. Our dust masses are lower than the value ( $0.5 \pm 0.1 M_{\oplus}$ ) derived by Moór et al. (2013) who only used the  $500\ \mu\text{m}$  flux for mass estimation. As described in Section 2.1, faint background galaxies within  $40''$  of the source are likely to contaminate the submillimeter fluxes. A better estimate of the disk mass will

have to come from high spatial resolution data like those from ALMA.

We used non-icy grains for the warm component with  $a_{min} = 2.2$ ,  $a_{max} = 1000\ \mu\text{m}$ , and  $q = 3.65$ . Because the warm component is less constrained, the uncertainty from the SED fitting is large. Assuming a flat disk density distribution, the warm component with radii ranging from  $\sim 7$  to  $\sim 10\ \text{AU}$  gave a consistent fit to the shape of the IRS spectrum. Alternatively, a Gaussian ring centered at  $8\ \text{AU}$  with a width of  $2\ \text{AU}$  resulted in a similar fit. The derived dust fractional luminosity is  $1.5 \times 10^{-4}$  with a total dust mass of  $\sim 4\text{--}5 \times 10^{-5} M_{\oplus}$ . The model SED of the two (warm and cold) flat disks is shown in Figure 6a.

Although the two-component model gives an overall good fit to the observed SED, the model images using these parameters do not fit the observations. Figure 7a shows the difference image (observation – model) for the two-component disk model at  $70\ \mu\text{m}$ , where very negative values at the source position are evident. The extension of the cold disk derived from the observed SED (radius  $\lesssim 200\ \text{AU}$ ) implies that the cold disk should not have been resolved with *Herschel*'s resolution (FWHM of  $5''.6$  at best). We can obtain reasonable SED fits to the cold disk by extending it up to  $\sim 800\ \text{AU}$ ; however, the surface density distribution has to have a steeper drop-off ( $r^{-1.5}$  compared to a flat disk of  $r^0$ ). This very wide planetesimal disk, perhaps analogous to the Solar System's scattered disk of KBOs, could generate dust grains in-situ from collisions. Using a uniform particle size distribution ( $a^{-3.5}$ ) at all astro-centric distances up to  $\sim 800\ \text{AU}$ , the resultant model images from such a wide disk with a steep radial gradient of surface density ( $\sim r^{-1.5}$ ) are similar to the ones using much smaller outer disk radii, i.e., not resolved. In order to account for the detected far-infrared emission at large astro-centric distances up to  $\sim 800\ \text{AU}$ , an extended component composed of only small dust grains on unbound or barely

bound orbits (i.e., a disk halo) is our best alternative. These small grains are most likely generated in the cold belt which may include a very wide scattered disk structure. However, given that the source is only resolved at  $\lesssim 1.4$  beams, no meaningful constraint can be placed based on the images.

Without some information on the brightness of the planetesimal belt, there is a wide range of parameters in this three-component SED model that can produce satisfactory fits. For example, if we assume the contribution of the planetesimal belt in the SED is roughly equal to the point source fluxes that are scaled to match the peak fluxes of the PACS images for subtraction, we are able to construct a three-component model that fits the overall SED (Figure 6b) and the far-infrared images. In this three-component model, the warm component is assumed to be the same as the two-component model (it has negligible contribution at far-infrared), and the emission at far-infrared is partitioned into the planetesimal belt (blue line in Figure 6b) and disk halo (red line in Figure 6b). The planetesimal-belt component has a dust fractional luminosity of  $\sim 8 \times 10^{-4}$  and a total dust mass of  $\sim 0.2 M_{\oplus}$  while the disk halo component has one third ( $\sim 3 \times 10^{-4}$ ) of the fractional luminosity in the planetesimal-belt component, but only  $\sim 10\%$  of the dust mass as a result of the disk halo being composed of  $\sim \mu\text{m}$  size grains. Figure 7b shows a detailed comparison between the observed and three-component model images at  $70 \mu\text{m}$ . Overall, the residual suggests the three-component model agrees with the observation within  $\pm 2\sigma$ .

## 4. DISCUSSION

### 4.1. The Nature of the Warm Component

Due to the large distance of HD 95086, the warm excess is inferred from the SED only, unlike for other nearby debris systems (Vega and Fomalhaut (Su et al. 2013), and  $\epsilon$  Eri (Backman et al. 2009)) where the warm and cold components are spatially separated. Recently, Kennedy & Wyatt (2014) presented an informative way to examine the properties of two-temperature disks, and tested the hypothesis that emission from a single narrow belt can account for the two observed temperatures by varying the particle size distribution. They conclude that the one-narrow-belt scenario is unlikely to produce two observed dust temperatures around early-type stars if the blowout size is preserved. Furthermore, the derived temperature and fractional luminosity ratios between the HD 95086 warm and cold components ( $R_T \sim 3.2$  and  $R_{f_d} \sim 0.1\text{--}0.2$ ) are located right at the center of the  $R_T$  vs.  $R_{f_d}$  plot (Figure 5 in Kennedy & Wyatt 2014), indicating that varying the particle size distribution in a narrow belt is unlikely to explain the observed SED.

Another possibility is that the warm excess emission could result from the small amount of particles being dragged in due to P-R drag. The effect of P-R drag in collisional dominated debris disks has been studied analytically by Wyatt (2005). In the case of the HD 95086 disk (a planetesimal belt at  $\sim 100$  AU with  $f_{d,cold} \sim 10^{-3}$  producing excess emission at  $\sim 10$  AU), the maximum amount of material available due to P-R drag in terms of optical depth is  $< 0.05 f_{d,cold}$ . Furthermore, the analytical maximum value was found to be a factor of  $\sim 7$  higher

than using a numerical model with a better treatment of collisional effects (van Lieshout et al. 2014). Thus, the observed value  $f_{d,warm} \sim 1.5 \times 10^{-4}$  for the warm component, is a factor of 20 higher than the maximum value that the cold belt can supply due to P-R drag, making this hypothesis unlikely. We, therefore, consider the warm component as an independent belt in the following discussion.

### 4.2. Detection of the $69 \mu\text{m}$ Forsterite Feature

The  $69 \mu\text{m}$  emission band, a solid state feature originating from magnesium-rich olivine crystals, was first observed astronomically by *ISO* around a Herbig Ae/Be star, HD 100546 (Malfait et al. 1998). The peak position and strength (FWHM) of the  $69 \mu\text{m}$  feature strongly depends on the iron content of the crystals and their temperatures (Bowey et al. 2002; Koike et al. 2003; Suto et al. 2006). See Sturm et al. (2013) and Maaskant et al. (2014) for recent reviews on the iron content and temperature dependence, and other secondary effects like grain sizes and shapes. The feature detected in the HD 95086 MIPS-SED data is not spectrally resolved, we cannot put constraints on the fraction of iron composition as has been done for  $\beta$  Pic (de Vries et al. 2012); however the iron fraction has to be less than a few % to have the feature peaked at  $69 \mu\text{m}$  at  $\sim 50$  K.

To further validate the detection of the forsterite  $69 \mu\text{m}$  feature and derive a rough estimate of the crystalline abundance, we took the mass absorption coefficients of synthetic forsterite (Fo100 in Koike et al. 2003), and constructed simple model fits to the MIPS-SED data. The model has two components: (1) emission from the crystalline forsterite and (2) a blackbody emission representing the underlying dust continuum, with both at the temperature of 55 K derived for the cold component. The model spectrum was smoothed to match the MIPS-SED resolution, and the ratio between the two components was adjusted to fit the overall shape of the MIPS-SED data. Since we do not have information about the location where the  $69 \mu\text{m}$  feature originates, the temperature of this component is not necessarily the same as that of the cold disk (underlying continuum). However, we can easily rule out the possibility that these crystalline grains originate from the warm belt with a dust temperature of  $\sim 175$  K since the blue part ( $50\text{--}60 \mu\text{m}$ ) of the model spectrum would have a much bluer slope. Given that the continuum in both blue and red sides of the feature is relatively flat, we assume the crystalline grains are located in the cold disk with the same dust temperature as the underlying continuum.

The upper panel of Figure 8 shows the best-fit model where the total mass of the forsterite component is  $\sim 6.2 \times 10^{25}$  g ( $0.01 M_{\oplus}$ ). Using the total dust mass we derived from the cold disk ( $0.2 M_{\oplus}$ , Section 3.2), the abundance of the crystalline grains is  $\sim 5\%$ . This abundance is likely to be a lower limit because the laboratory measured absorption coefficients are based on finely ground powder (sizes of  $0.1\text{--}0.5 \mu\text{m}$ ), and the  $69 \mu\text{m}$  feature is not sensitive to grain size (the band profiles are similar for grains less than  $\sim 10 \mu\text{m}$ , Sturm et al. 2013)<sup>4</sup>. Since

<sup>4</sup> The changes in the peak position and FWHM of the  $69 \mu\text{m}$  band profiles at different grain sizes are all much smaller than the spectral resolution of the MIPS-SED mode data.

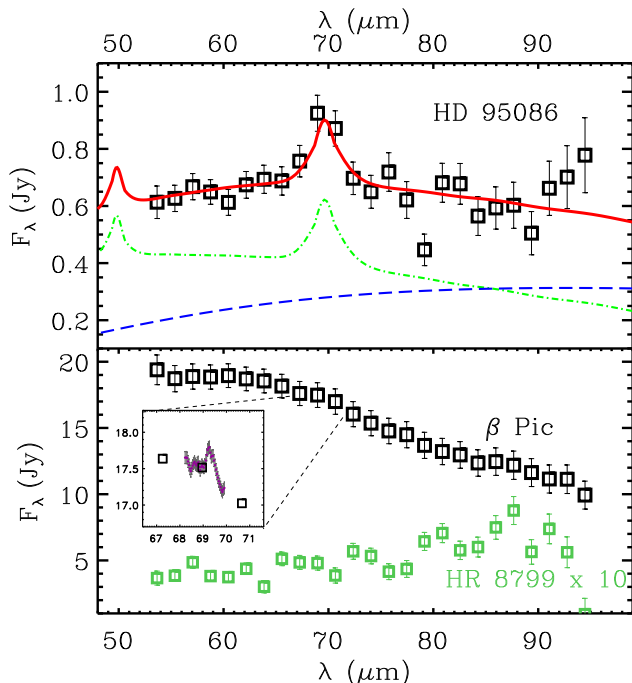


FIG. 8.— Photosphere-subtracted MIPS-SED data (open squares with error bars) for HD 95086 (upper panel),  $\beta$  Pic and HR 8799 (bottom panel). Our best-fit model, shown as the solid red line in the upper panel, consists of the underlying dust continuum (55 K blackbody emission, the blue dashed line) and the emission of crystalline forsterite (the green dotted-dashed line) after smoothing to match the MIPS-SED resolution. The MIPS-SED data of HR 8799 in the bottom panel was scaled by 10 times for easy comparison. The inset of the bottom panel shows the scaled (by 1.07) PACS spectroscopic data (purple line) from de Vries et al. (2012).

no prominent crystalline features are seen in the observed 20–40  $\mu\text{m}$  range (while our best-fit model predicts strong features), the crystalline grains must have sizes  $\gtrsim$  a few  $\mu\text{m}$ . Therefore, the derived abundance should be taken as a lower limit.

The presence of crystalline silicates at a low temperature and far from the star is surprising, given that relatively high temperatures are required to convert circumstellar amorphous silicates to the crystalline form (Fabian et al. 2000). The detection of the forsterite emission feature implies that there is a substantial transport of material from the inner zone of the system, or that material has been released from the disruption of a large body where high temperatures were reached during formation.

It is interesting to note that the 69  $\mu\text{m}$  feature was not detected in the MIPS-SED data of  $\beta$  Pic (the bottom panel of Figure 8), while the crystalline abundance is estimated to be  $3.6 \pm 1.0\%$  using the PACS spectroscopic data (de Vries et al. 2012). With the published PACS spectrum smoothed to match the MIPS-SED resolution, we found that the low equivalent width of the detected feature is completely washed out in the MIPS-SED mode (the inset of the bottom panel of Figure 8). This is also consistent with the derived mass values for the crystalline grains ( $2.8 \times 10^{23}$  g for the  $\beta$  Pic disk, while the mass we estimate for HD 95086 is  $\gtrsim 200$  times more). The estimated crystalline abundances implied by the observed feature strengths in these two systems appear discrepant. The discrepancy lies in the total dust

mass used to derive the abundance, which is model dependent. The SED models used for the  $\beta$  Pic system include grains up to 100  $\mu\text{m}$  for all three-temperature components (de Vries et al. 2012), while our models for HD 95086 include grains up to 1000  $\mu\text{m}$ , i.e., a factor of  $\sim 3$  in the derived dust mass in a typical  $a^{-3.5}$  size power law ( $M_d \sim \sqrt{a_{max}}$ ). Indeed, the total non-crystalline, derived dust mass by de Vries et al. (2012) is a factor of  $\sim 3$  lower than the value ( $4.7 \times 10^{26}$  g) derived from recent ALMA observation for  $\beta$  Pic (Dent et al. 2014). Furthermore, the reported 3.6% crystalline abundance is only based on one of the temperature components ( $\sim 90$  K with a total mass of  $8 \times 10^{24}$  g). Using the ALMA derived dust mass, the crystalline abundance in the  $\beta$  Pic disk should be  $\lesssim 1\%$ . As we compare the disk properties between HD 95086 and HR 8799 in the following subsection, it is also noteworthy that no feature was detected in the MIPS-SED data around HR 8799 (Figure 8) (Su et al. 2009), suggesting the crystalline abundance is  $< 1\%$ .

#### 4.3. Constraints on the Eccentricity of the Disk

The eccentricity,  $e$ , of debris disks usually can be measured in two ways: (1) the offset between the ring center and star position, and (2) the degree of asymmetry seen in thermal images (i.e., pericenter glow). Both methods have been applied to the Fomalhaut debris disk (Kalas et al. 2005; Stapelfeldt et al. 2004) and result in a consistent value ( $e \sim 0.1$ ). Since the star contributes negligibly in the PACS wavelengths, the centroid we measured from the PACS images is the center of the disk. Based on the calibration observations of the PSF star,  $\gamma$  Dra, a typical centroiding uncertainty is  $0''.01$ . The position of the star is well measured by 2MASS with a known proper motion from Hipparcos; therefore, the uncertainty in its position relative to the *Herschel* detection is dominated by the absolute accuracy of the World Coordinate Systems (WCS) in *Herschel*/PACS maps. We used a bright galaxy (LEDA 3079352, 2MASS J10571665-6838171) present in the field of our PACS images to estimate the absolute pointing uncertainty. There appears to be an offset of  $\sim 2''.2$  between the 2MASS and *Herschel* coordinate systems. The typical pointing uncertainty in *Herschel* observations ( $\sim 2''$ ) makes it difficult to pin point the star position with high accuracy (i.e., the first method is inapplicable).

We then turned to the second method to assess the degree of asymmetry we could have detected with *Herschel* observations. Since the resolved structure is mostly dominated by the disk halo (the planetsimal belt is not resolved at *Herschel*'s resolution), the presumption is that the disk halo shape follows closely with that of the planetsimal belt. This assumption is reasonable if the disk halo results from small grains generated in the parent-body belt that are ejected and/or placed in highly eccentric orbits due to radiation pressure. There appears to be some asymmetry seen in the PSF-subtracted images (bottom row of Figure 3); however, it is not significant (less than  $3\sigma$ ). The resolved component is consistent with the circular case with  $e = 0$  (our baseline model shown in Figure 6b and Figure 7b). We then constructed model images by placing the disk halo components at various eccentricities and compared them with our baseline

TABLE 1  
PROPERTIES COMPARISON BETWEEN HR 8799 AND HD 95086

	HR 8799		HD 95086	
Stellar Parameter				
$M_*$ [ $M_\odot$ ]	1.5		1.6	
$L_*$ [ $L_\odot$ ]	5.7		7.0	
$T_{eff}$ [K]	7500		7500	
$R_*$ [ $R_\odot$ ]	1.4		1.6	
age [Myr]	$\sim 30\text{--}90^{[1]}$		$\sim 20^{[2]}$	
distance [pc]	39.4		90.4	
SED Parameter				
	<i>warm</i>	<i>cold</i>	<i>warm</i>	<i>cold</i>
$T_d$ [K]	$\sim 150$	$\sim 45$	$\sim 175$	$\sim 55$
$f_d$	1.8E-5	2.2E-4	1.5E-4	1.5E-3
$M_d$ [ $M_\oplus$ ]	1E-6	0.1	5E-5	0.2–0.5
Disk Orientation				
$i$ [degree]	25 $\pm$ 5		25 $\pm$ 5	
P.A. [degree]	62 $\pm$ 10		115 $\pm$ 10	
Planet				
	e, d, c, b		b	
$M_p$ [ $M_J$ ]	9 $\pm$ 2, 9 $\pm$ 3, 9 $\pm$ 3, 7 $\pm$ 2 <sup>[3]</sup>		5 $\pm$ 2 <sup>[4]</sup>	
$a_p$ [AU]	15.4, 25.4, 39.4, 69.1		61.5 $^{+5.7}_{-4.9}$ <sup>[5]</sup>	

REFERENCES. — [1] Baines et al. (2012), see Sec 4.4 for details; [2] Meshkat et al. (2013); [3] Goździewski & Migaszewski (2014); [4] Rameau et al. (2013b); [5] this work, assuming  $e_b=0$ .

model. We found that the difference is noticeable (more than  $5\sigma$ ) when  $e > 0.25$ . From this exercise, we conclude that the resolved structure (disk halo) around HD 95086 has  $e < 0.3$ .

#### 4.4. Is HD 95086 A Young Analog of HR 8799?

Given that both HR 8799 and HD 95086 have bright debris disks and wide-orbit planets revealed via direct imaging, it is instructive to compare their properties in regard to different aspects of the planetary configuration. Table 1 lists the properties of the HR 8799 and HD 95086 systems. The debris structures revealed from excess SEDs and resolved images show that both systems have a warm ( $\sim 170$  K) excess near the water-ice line and a cold excess at  $\sim 50$  K, surrounded by an extended disk halo. The HD 95086 system is  $\sim 10$  times dustier than the HR 8799 in terms of fractional dust luminosity, but the ratio of fractional luminosities of the warm and cold components is similar ( $\sim 0.1$ ). The extended disk halo in HR 8799 can be traced up to  $\sim 2000$  AU with a sensitivity of  $10^{-2}$  mJy arcsec<sup>2</sup> (Matthews et al. 2014); interestingly, a similar size is seen in the HD 95086 system with the same detection limit, implying its disk halo is  $>5$  times brighter given that it is  $\sim 2.3$  times more distant. Based on the resolved images, Matthews et al. (2014) estimated the HR 8799 disk halo accounts for 40%, 46% and 52% of the total flux at 70, 100 and 160  $\mu\text{m}$ , respectively. In the case of HD 95086, the marginally resolved images can only give a lower limit for the contribution from the disk halo, which is  $\gtrsim 42\%$ ,  $\gtrsim 39\%$  and  $\gtrsim 27\%$  at 70, 100 and 160  $\mu\text{m}$ , respectively. In other words, the debris structures in these two systems are very similar except that the debris in the HD 95086 system is  $\sim 10$  times more in dust luminosities and 2–5 times more in observed dust masses (derived from SED fitting) compared to those values in the HR 8799 system.

That both systems are of 10–100 Myr age is exciting

because this is the epoch when interesting processes like dynamical settling, formation of rocky planets, and possibly even (late) formation of ice giants are expected to occur in planetary systems. The age estimate of HD 95086 ( $\sim 20$  Myr) is quite robust given its association with the LCC moving group; but the age of HR 8799 has been widely debated. Most of the dating methods applicable for early-type stars favor an age younger than  $\sim 150$  Myr (Marois et al. 2008), while asteroseismic analysis based on the ground-based data favors an older age of  $\sim 1$  Gyr (Moya et al. 2010). Recent optical monitoring using the Microvariability and Oscillations in STars (MOST) space data found significant frequency and amplitude changes in HR 8799’s pulsation, making precise asteroseismic analysis difficult (Sódor et al. 2014). The age of HR 8799 was revisited by Baines et al. (2012) with the directly measured stellar diameter from interferometric CHARA data and evolutionary models, who derived two age estimates:  $33^{+7}_{-13.2}$  Myr if the star is still contracting toward the zero-age main sequence (ZAMS), and  $90^{+381}_{-50}$  Myr if the star is evolving from ZAMS. Therefore, it is possible that HR 8799 could be as young as HD 95086 (20 Myr), but it is more likely older, by up to  $\gtrsim 10$  times.

If both HR 8799 and HD 95086 are at the same age, the difference in the observed dust level must reflect different initial conditions. Based on the evolution models of debris disks developed by Kenyon & Bromley (2008), the relative disk luminosity ( $f_d$ ) around a  $2 M_\odot$  star at age of 20 Myr can be up to 10 times higher if one disk started with 10 times more mass than the other (Figure 17 in that paper). This suggests that HR 8799 was born with a less massive protoplanetary disk than that of HD 95086 if both have the same age. However, all four directly imaged planets in the HR 8799 system are  $\sim 2$  times more massive than the HD 95086 planet, implying the opposite trend in initial conditions. Alternatively, if both systems formed with similar initial conditions (mass and angular momentum), the difference in the dust level must be related to debris evolution. The models by Kenyon & Bromley (2008) predict the decline in disk luminosity is roughly a power law,  $f_d \propto t^{-n}$  with  $n \approx 0.6\text{--}1.0$ . With possible ages of 40–200 Myr for HR 8799, the differences in  $f_d$  between HD 95086 and HR 8799 suggest  $n \sim 1.0\text{--}3.3$ , a steeper decline than the model prediction.

Perhaps the biggest difference between these two systems is that HR 8799 hosts four massive (7–9  $M_J$ ) planets between the warm and cold belts, while there is only one  $\sim 5 M_J$  planet currently known that is just interior to the HD 95086 cold belt. Because HD 95086 is more than two times more distant than HR 8799, the current direct imaging observations are only sensitive to  $\gtrsim 5 M_J$  as close as  $\sim 30$  AU to the star (Rameau et al. 2013a). Similar to the well-resolved two-belt systems (HR 8799, Vega, Fomalhaut and  $\epsilon$  Eri), the large gap between the warm and cold excesses might host multiple planets.

#### 4.5. Dynamical Constraints on Possible Planet Configurations

We can constrain possible planet configurations of the HD 95086 system based on two dynamical considerations: (1) multiple planets must be dynamically stable for a time span of the age of the HD 95086 sys-

tem,  $\sim 20$  Myr, and (2) the planets’ gravitational perturbations must clear and maintain the gap between the warm and cold belts. For the former, we make use of the numerical results of Faber & Quillen (2007) on the stability of multiple planet systems in coplanar configurations of roughly geometrically spaced orbits. For the latter we make use of numerical estimates of a planet’s chaotic zone in which debris can be cleared and a gap can be maintained by each planet. The chaotic zone is owed to the overlap of first order mean motion resonances, as shown by Wisdom (1980), who estimated the chaotic zone width as  $\Delta a \simeq 1.3\mu^{\frac{2}{7}}a_p$ , where  $\mu = M_p/M_*$ , and  $M_p, a_p$  are the planet’s mass and orbital semi-major axis. In this zone, initially circular test particle orbits exhibit strongly chaotic motion. Subsequent numerical studies have supported this estimate for planet-to-star mass ratios,  $\mu$ , up to about  $10^{-3}$  (Duncan et al. 1989). Morrison & Malhotra (2014) carried out numerical integrations for  $\mu$  up to  $10^{-1.5}$ , to determine the range in the planet’s chaotic zone where particles are not merely chaotic, but actually cleared (by either collision or escape); they report cleared zone widths, both interior and exterior to a planet’s circular orbit, as follows:  $\Delta a_{cl,int} = 1.2\mu^{0.28}a_p$  and  $\Delta a_{cl,ext} = 1.7\mu^{0.31}a_p$ . In this section, we use these “cleared zone” widths to estimate the effects of planets on the clearing of debris. However, we continue to refer to these as “chaotic zone” widths, to acknowledge the underlying dynamical mechanism of clearing. Below, we consider possible planetary systems in coplanar, non-resonant configurations.

#### 4.5.1. Single Planet System

Could HD 95086b alone be responsible for the gap,  $\sim 8$  AU to  $\sim 80$  AU, between the warm and the cold belts? HD 95086b’s estimated mass,  $5 \pm 2M_J$ , and its observed location imply that it orbits within the gap and that it is at least shepherding the inner edge of the cold belt. The projected astro-centric distance of HD 95086b of  $55.7 \pm 2.5$  AU and the disk inclination angle of  $25^\circ \pm 5^\circ$  yield a de-projected distance,  $r_b = 61.5^{+5.7}_{-4.9}$  AU. The separation of the planet from the inner edge of the cold belt is  $\sim (80 - r_b) \approx (13-23)$  AU. For the nominal planet mass,  $M_b = 5M_J$ , and nominal circular orbit of radius  $a_b \approx 61.5$  AU, this separation distance is similar to the expected range,  $\Delta a_{cl,ext} = 1.7(M_b/M_*)^{0.31}a_b \approx 17$  AU, of clearing of test particles in the planet’s chaotic zone exterior to its orbit.

To be responsible for the whole gap, the planet would have to be on a highly eccentric orbit, with apocenter near its present location, and pericenter near the warm belt (actually near one chaotic zone width removed from the warm belt), i.e., with an orbital eccentricity  $e_b \approx 0.7$ . Such a high eccentricity of the planet’s orbit would then force a high eccentricity on the debris belts too. The eccentricity of the debris belts are undetermined from the current observations; therefore, it cannot be ruled out that HD 95086b on an eccentric orbit may be the cause of the large gap between the warm and cold belts. However, it begs the question of how HD 95086b would have gained such a highly eccentric orbit. It is more plausible that multiple planets exist in this large gap.

#### 4.5.2. Two Planet System

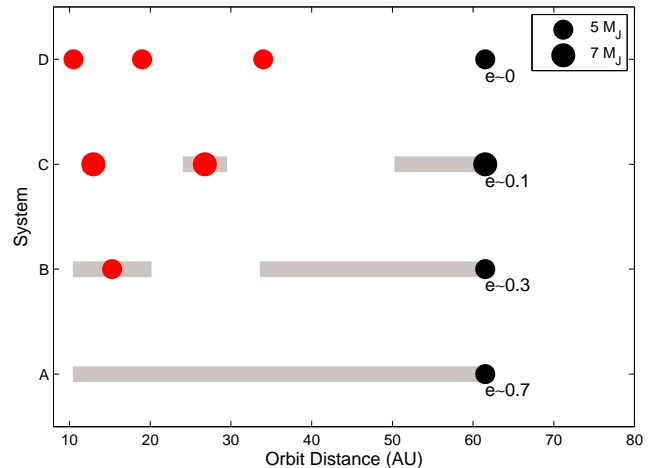


FIG. 9.— Possible planetary architectures of HD 95086 that are dynamically stable or marginally stable for the age of the system and that can also account for the gap between the warm and cold debris belt. The black points show the nominal location and mass of HD 95086b; red points indicate the semi-major axis of hypothetical (unseen) planets; the grey bars indicate the possible range of astro-centric distances of each planet, in the systems with eccentric orbits. Size of points indicate planet mass.

Let us consider whether the gap could be maintained by two planets on low eccentricity ( $e \sim 0.1$ ) orbits. The known planet, HD 95086b, of mass  $\sim 5 \pm 2 M_J$  on a nearly circular orbit of radius  $\sim 61.5 \pm 5$  AU would both shepherd the outer belt as well as clear debris inward of its orbit by about one chaotic zone width, i.e. down to about 42 AU at most. The second unseen planet must be located near the inner belt. Assuming that this planet is of mass  $\sim 13 M_J$  (the conventional upper limit of planetary masses), and its pericenter is located one chaotic zone width ( $\Delta a_{cl,int}$ ) away from the outer edge of the inner belt, we estimate that its semi major axis is  $\sim 13$  AU. Such a putative planet could shepherd the inner belt and clear debris out to a maximum distance of about 18 AU. This is insufficient to account for the entire 8–80 AU observed gap. We can also consider a higher mass, unseen sub-stellar object near the inner belt. Currently, the best detection limit ( $5\sigma$ ) for low-mass companions close to the star is  $\sim 21M_J$  at a astro-centric distance of  $0''.18$  ( $\sim 16$  AU) (Meshkat et al. 2014). Demanding that a  $21M_J$  object be able to shepherd the inner belt edge at  $\sim 8$  AU implies that its pericenter is located at about one chaotic zone width away, i.e., at about 14 AU. This means that it can clear debris out to about  $(14 + \Delta a_{cl,ext}) \approx 20$  AU. This is also insufficient to account for the entire 8–80 AU gap. We conclude that two planets on low eccentricity orbits are unable to account for the gap.

If we relax the low eccentricity condition, then it is possible to account for the gap provided one or both planets’ orbits are of significant eccentricity. First, let’s consider that HD 95086b is of low eccentricity but the inner unseen planet is of high eccentricity. Then, as we noted above, HD 95086b can clear debris inward of its orbit to about  $\sim 42$  AU astro-centric distance, so we require the inner unseen planet to account for debris clearing in the range 8–42 AU. Adopting the maximum mass for the inner planet,  $M_1 = 13M_J$ , we can estimate its pericenter and apocenter distances:  $q_1 \simeq 8/(1 - 1.2(M_1/M_*)^{0.28}) \simeq 12$  AU, and  $Q_1 \simeq 42/(1 +$

$1.7(M_1/M_*)^{0.31} \simeq 30$  AU. Therefore, the inner planet (of maximum planet mass  $13M_J$ ) must have orbital eccentricity  $\sim 0.5$  to account for the observed gap. Solutions with somewhat lower planet mass and eccentricity are possible. For example, consider two planets of similar mass,  $5M_J$ , and similar orbital eccentricity,  $\sim 0.3$ , with the inner planet’s orbit of semi major axis  $\sim 16$  AU and HD 95086b’s orbit of semi major axis  $\sim 40$  AU. Their pericenter and apocenter distances, augmented with one chaotic zone width each, could shepherd the warm and cold belt edges as well as clear the 8–80 AU gap; moreover, the planets’ orbits are also marginally stable for the 20 Myr age of the system. This two-planet configuration is illustrated in Figure 9 as “system B”.

#### 4.5.3. Three Planet System

Given the young age of this system, it is plausible that the gap contains multiple (more than two) planets in orbits that are only marginally stable on  $\sim 20$  Myr timescales. The parameter space of such multiple-planet configurations is very large, of course. To obtain some rough estimates, we consider systems of three and four planets, with equal-mass planets on coplanar low eccentricity ( $e < 0.1$ ) orbits, and demand stability for only  $\sim 20$  Myr. Then we identify a few possible configurations as follows.

In a putative three-planet system, let’s designate the three planets with index 1, 2, 3 in order of increasing astro-centric distance. Planet 1 is identified with the one that must shepherd the outer edge of the warm belt (located at  $\sim 8$  AU), while planet 3 is identified with the detected planet, HD 95086b (currently located at astro-centric distance  $r_b \approx 61.5 \pm 5$  AU). Then, the pericenter distance of planet 1,  $q_1 = a_1(1 - e_1)$ , must be approximately one chaotic zone width ( $\Delta a_{cl,int}$ ) away from the edge of the warm belt, i.e.  $q_1 \approx 8/(1 - 1.2\mu_1^{0.28})$  AU where  $\mu_1 = M_1/M_*$  is the planet-to-star mass ratio. Adopting the 1- $\sigma$  upper limit of the mass of planet b ( $7 M_J$ ) for the equal-mass planet 1, and  $e_1 = 0.1$ , we find that  $a_1 \simeq 12$  AU. For planet b, assuming it is currently near apocenter and that it has orbital eccentricity  $e_b = 0.1$ , we find  $a_3 \simeq 56 \pm 5$  AU. To estimate the orbit of planet 2, let’s assume that its fractional separation from planet 1 is the same as from planet 3, i.e.,  $a_2 = a_1(1 + \delta) = a_3/(1 + \delta)$ ; this yields  $\delta \simeq 1.16$  and thereby  $a_2 \simeq 26$  AU. We then ask if this three-planet configuration is dynamically stable for a time span of  $\sim 20$  Myr, which is about  $10^6$  orbital periods of the innermost planet. Referring to the pertinent numerical study of Faber & Quillen (2007) who investigated dynamical stability of multiple planets in coplanar low eccentricity orbits of equal fractional separations, we find that  $\delta = 1.16$  exceeds by a comfortable margin the minimum value,  $\delta_{min} \simeq 3.5\mu^{1/4} \simeq 0.9$  for  $\mu = 7M_J/1.6M_\odot = 0.00418$ , required for dynamical stability for a time span of  $10^6$  orbital periods of the innermost planet. Hence, this three  $7M_J$  planet system is dynamically stable for  $\sim 20$  Myr.

We then ask if this planet configuration may account for the entire 8–80 AU gap. By construction, planet 1 and planet 3 shepherd the edges of the warm and cold belts, respectively. We calculate that the exterior chaotic zone of planet 1 (measured from its apocenter) just marginally overlaps the interior chaotic zone of planet

2 (measured from its pericenter); similarly, the exterior chaotic zone of planet 2 (measured from its apocenter) just overlaps the interior chaotic zone of planet 3 (measured from its pericenter). Thus, within the observational uncertainties, we consider that this configuration of three equal-mass planets, each of mass  $7M_J$ , in low eccentricity orbits of semi major axes  $\sim 12$  AU, 26 AU and 56 AU, is stable for the age of the system and can also (marginally) account for the entire gap between the warm and cold belts. This three-planet configuration is illustrated in Figure 9 as “system C”. We note that three planets of much smaller mass (or of vanishingly small orbital eccentricities) would be less likely to meet the observational constraint of maintaining the large gap. Thus, we are motivated to consider a four planet system of lower mass planets.

#### 4.5.4. Four Planet System

In a putative four, equal-mass, we designate the four planets with index 1, 2, 3, 4 in order of increasing astro-centric distance. As above, planet 1 is identified with the one that must shepherd the outer edge of the warm belt (located at  $\sim 8$  AU), while planet 4 is identified with the detected planet, HD 95086b (currently located at astro-centric distance  $r_b \approx 61.5 \pm 5$  AU). Assuming circular orbits, planet 1 must be approximately one chaotic zone width ( $\Delta a_{cl,int}$ ) away from the edge of the warm belt, i.e.  $a_1 \approx 8/(1 - 1.2\mu_1^{0.28})$  AU; adopting the nominal mass of planet b ( $5 M_J$ ) for the equal-mass planet 1, we find that  $a_1 \simeq 11$  AU. For planet b, we have  $a_b \simeq (61.5 \pm 5)$  AU. We assume that the adjacent planets’ fractional orbital separations are equal, i.e.,  $a_{j+1} = a_j(1 + \delta)$ . We calculate  $\delta = (a_b/a_1)^{1/3} - 1 \simeq 0.8$  and thereby  $a_2 \simeq 19$  AU and  $a_3 \simeq 34$  AU. Again, referring to the results of Faber & Quillen (2007), we calculate that  $\delta_{min} = 3.5\mu^{1/4} \simeq 0.82$  for  $\mu = 5M_J/1.6M_\odot = 0.003$ . Thus, our putative four planet configuration is likely just marginally stable for the age of the system. We then ask if this orbital configuration may account for the entire 8–80 AU gap. By construction, planet 1 and planet b shepherd the edges of the warm and cold belts, respectively. We calculate that, for circular planetary orbits, the exterior chaotic zone of planet 1 extends to  $\sim 13$  AU, the interior chaotic zone of planet 2 extends to  $\sim 14$  AU, the exterior chaotic zone of planet 2 extends to  $\sim 24$  AU, the interior chaotic zone of planet 3 extends to  $\sim 26$  AU, the exterior chaotic zone of planet 3 extends to  $\sim 44$  AU. Thus, within the observational and theoretical uncertainties, we consider that this configuration of four equal-mass planets, each of mass  $5 M_J$ , in nearly circular orbits of semi-major axes 11 AU, 19 AU, 34 AU and 62 AU, can account for the entire gap between the warm and cold belts, and is also just marginally stable for the age of the system. This four-planet configuration is illustrated in Figure 9 as “system D”. We note that a four-planet system is unlikely to be stable if the planet masses exceed  $\sim 5 M_J$ . We also note that HR 8799 planets are not stable under these stability criteria; Goździewski & Migaszewski (2014) propose a multiply resonant orbital configuration to ensure dynamical stability of this system. Similarly, higher mass, coplanar planetary configurations of four planets in HD 95086 could be stable if the orbital parameters were fine-tuned

to involve mean motion resonances.

For the directly-imaged four-planet system of HR 8799, a massive cold debris disk exceeding 10% of the outermost planet’s mass has been suggested to stabilize otherwise unstable configurations for several Myr (Moore & Quillen 2013). In the case of HD 95086, the mass of the cold debris belt in particles up to 1 mm size is  $\sim 0.2 M_{\oplus}$ ; extrapolating to km-size bodies using a  $-3.5$  size power-law yields a total cold disk mass of  $\sim 200 M_{\oplus}$ . If this debris disk mass estimate is robust, the cold disk might play a role in stabilizing a dynamically packed planetary system with multiple massive planets similar to that of HR 8799.

## 5. CONCLUSIONS

We present a detailed study of the debris disk around HD 95086, a young star that also harbors a directly imaged planet. We find:

1.) The observed disk SED of HD 95086 is best described with two dust temperatures: a warm component at  $\sim 175$  K and a cold component at  $\sim 55$  K. There is a possible hotter, but much fainter component at  $\sim 300$  K, suggesting the presence of debris in the terrestrial planet zone that needs future confirmation.

2.) We detect an emission feature in the low-resolution MIPS-SED data. The feature peaks at  $69.5 \pm 0.5 \mu\text{m}$ , and is not spectrally resolved. Its integrated luminosity and peak wavelength are consistent with a mineralogical feature originating from iron-poor, crystalline olivine that has been detected in many protoplanetary disks and in the  $\beta$  Pic debris disk. HD 95086 is the second debris disk, after  $\beta$  Pic, to show a feature. We estimate the mass of crystalline grains to be  $\sim 6.2 \times 10^{25}$  g, accounting for  $\sim 5\%$  abundance in the observed dust debris. Because of the high temperature of crystallization, the substantial mass required to produce this feature must have been transported from regions close to the star, or heated in the core of a planetary body that have been disrupted. The latter is consistent with the fact that this feature only detected in dustiest systems in young debris disks where collisional rates are high.

3.) Detailed analysis of the far-infrared resolved images suggests the debris emission can be traced up to radii of  $\sim 9''$  (800 AU) where  $\sim$ half of the emission is within the beam size (radii  $\lesssim 250$  AU) and not resolved. Our SED models suggest that the cold component has an outer boundary (radius) less than 200 AU, contradicting our imaging analysis. To reconcile the SED models and the extended emission, a third component in the SED models is needed. The extended third component is likely to be a disk halo, similar to the ones that have been found in Vega and HR 8799 (Su et al. 2005, 2009; Matthews et al. 2014), made of grains closer to or smaller than the blowout size that stellar radiation pressure places them in highly eccentric or hyperbolic orbits. We confirm previous determinations that the resolved structure is at an inclination of  $25^\circ \pm 5^\circ$  and a position angle of  $115^\circ \pm 10^\circ$ , and find that the eccentricity of the disk halo is small,  $e < 0.3$ .

4.) We compare the derived properties of the three components in HD 95086 to those of HR 8799 (Su et al. 2009), and find a striking similarity in debris structures. Both systems possess warm and cold excesses with an orbital ratio of  $\sim 10$ , similar to the ratios between Aster-

oid and Kuiper belts in our Solar System and some extrasolar debris disks (Su et al. 2013; Kennedy & Wyatt 2014). Most importantly, both HD 95086 and HR 8799 systems also possess a bright disk halo, suggesting an elevated level of activities in the leftover planetesimals. It is interesting to note that the difference in dust level (fractional luminosity) is  $\sim 10$  times in both warm and cold excesses between HD 95086 and HR 8799 where HD 95086 is dustier.

5.) We explore the possible planetary configurations present in the HD 95086 system using dynamical constraints from the debris distribution and currently known  $5 M_J$  planet at a astro-centric distance of 61.5 AU in coplanar cases. For the case of a single planet system, the eccentricity of HD 95086b is required to be  $\approx 0.7$  to maintain the large gap. Although we cannot rule out the single planet case, the origin of its high eccentricity requires an additional explanation. For the case of a two-planet system, the current mass limit ( $21 M_J$  at a astro-centric distance of  $\sim 16$  AU) rules out two planets on low eccentricity ( $e < 0.1$ ) orbits; however, two  $5 M_J$  planets on modest ( $e \sim 0.3$ ) eccentricity orbits are marginally stable for  $\sim 20$  Myr and can maintain the large gap.

6.) We further estimate the stability of packed configurations for three and four equal-mass planets on low eccentricity ( $e < 0.1$ ) orbits. In the case of three planets, the planets need to be as massive as  $7 M_J$  (the maximum mass for HD 95086b) and at semi-major axes of  $\sim 12$  AU, 26 AU, and 56 AU to be dynamically stable and to maintain the gap. Three planets of much smaller mass would be less likely to maintain the large gap. We also show that the HD 95086 system could host four low-eccentricity, massive planets between its warm and cold belts, similar to the iconic HR 8799 system; however, barring fine-tuning with mean motion resonances, these four planets would have masses  $\lesssim 5 M_J$  in order to be stable over the system’s age ( $\sim 20$  Myr).

Finally, our results also illustrate resolved imaging (even marginally resolved in this case) can provide much more insight if accompanied by proper SED modeling. Since both HD 95086 and HR 8799 systems are in the epoch when active dynamical processes like final settling of giant planet migration and terrestrial planet formation are in play, the observed difference in the dust level probably reflects the age difference, i.e., HD 95086 is a younger analog of HR 8799, rather than initial conditions. Future higher sensitivity data in the properties of the debris components will provide a better time resolution in this active planet formation epoch. Among the currently known 9 directly imaged extrasolar planets<sup>5</sup> (masses less than  $13 M_J$ ), the host stars also possess bright debris disks except for GJ 504, implying a strong connection between bright debris disks and directly imaged planets. The demography of planetary systems revealed by indirect methods (radial velocity, transit, micro-lensing and presence of debris) suggests the formation and evolution of planetary systems have multiple paths. Therefore, finding common features among planetary systems is the first step to better understand

<sup>5</sup> HR 8799 bcde: Marois et al. (2010), Fomalhaut b: Kalas et al. (2008),  $\beta$  Pic: Lagrange et al. (2009), HD 95086 b: Rameau et al. (2013a), GJ 504 b: Kuzuhara et al. (2013), HD 106906 b: Bailey et al. (2014).

their formation and evolution.

We thank the anonymous referee for his/her rapid report and suggestions led to a better presentation of the paper. We thank B. de Vries for providing the PACS spectrum of  $\beta$  Pic. KYLS acknowledges the sup-

port provided by the NASA Astrophysics Data Analysis Program through grant # NNX11AF73G. SJM acknowledges funding from NASA grants #NNX13AO65H and #NNX14AG93G. RM acknowledges funding from NASA grant #NNX14AG93G and NSF grant #AST-1312498. ZB is funded by the Deutsches Zentrum für Lufund Raumfahrt (DLR).

#### REFERENCES

- Backman, D., Marengo, M., Stapelfeldt, K., et al. 2009, *ApJ*, 690, 1522
- Ballering, N. P., Rieke, G. H., Su, K. Y. L., & Montiel, E. 2013, *ApJ*, 775, 55
- Ballering, N. P., Rieke, G. H., & Gáspár, A. 2014, *ApJ*, 793, 57
- Bailey, V., Meshkat, T., Reiter, M., et al. 2014, *ApJ*, 780, L4
- Baines, E. K., White, R. J., Huber, D., et al. 2012, *ApJ*, 761, 57; CHARA
- Balog, Z., Müller, T., Nielbock, M., et al. 2014, *Experimental Astronomy*, 37, 129
- Bowey, J. E., Barlow, M. J., Molster, F. J., et al. 2002, *MNRAS*, 331, L1
- Burke, C. J., Bryson, S. T., Mullally, F., et al. 2014, *ApJS*, 210, 19
- Chen, C. H., Sargent, B. A., Bohac, C., et al. 2006, *ApJS*, 166, 351
- Chen, C. H., Sheehan, P., Watson, D. M., Manoj, P., & Najita, J. R. 2009, *ApJ*, 701, 1367
- Chen, C. H., Pecaut, M., Mamajek, E. E., Su, K. Y. L., & Bitner, M. 2012, *ApJ*, 756, 133
- Chen, C. H., Mittal, T., Kuchner, M., et al. 2014, *ApJS*, 211, 25
- Dent, W. R. F., Wyatt, M. C., Roberge, A., et al. 2014, *Science*, 343, 1490
- Duncan, M., Quinn, T., & Tremaine, S. 1989, *Icarus*, 82, 402
- Faber, P., & Quillen, A. C. 2007, *MNRAS*, 382, 1823
- Fabian, D., Jäger, C., Henning, T., Dorschner, J., & Mutschke, H. 2000, *A&A*, 364, 282
- Galicher, R., Rameau, J., Bonnefoy, M., et al. 2014, *A&A*, 565, L4
- Gáspár, A., Psaltis, D., Rieke, G. H., Özel, F. 2012, *ApJ*, 754, 74
- Golimowski, D. A., Ardila, D. R., Krist, J. E., et al. 2006, *AJ*, 131, 3109
- Goździewski, K., & Migaszewski, C. 2014, *MNRAS*, 440, 3140
- Heap, S. R., Lindler, D. J., Lanz, T. M., et al. 2000, *ApJ*, 539, 435
- Higdon, S. J. U., Devost, D., Higdon, J. L., et al. 2004, *PASP*, 116, 975
- Kalas, P., Graham, J. R., & Clampin, M. 2005, *Nature*, 435, 1067
- Kalas, P., Graham, J. R., Chiang, E., et al. 2008, *Science*, 322, 1345
- Kennedy, G. M., & Wyatt, M. C. 2014, *MNRAS*, 444, 3164
- Kenyon, S. J., & Bromley, B. C. 2008, *ApJS*, 179, 451
- Koike, C., Chihara, H., Tsuchiyama, A., et al. 2003, *A&A*, 399, 1101
- Kuzuhara, M., Tamura, M., Kudo, T., et al. 2013, *ApJ*, 774, 11
- Lagrange, A.-M., Gratadour, D., Chauvin, G., et al. 2009, *A&A*, 493, L21
- Laor, A., & Draine, B. T. 1993, *ApJ*, 402, 441
- Lebouteiller, V., Bernard-Salas, J., Sloan, G. C., & Barry, D. J. 2010, *PASP*, 122, 231
- van Leeuwen, F. 2007, *A&A*, 474, 653
- van Lieshout, R., Dominik, C., Kama, M., & Min, M. 2014, arXiv:1404.3271
- Lu, N., Smith, P. S., Engelbracht, C. W., et al. 2008, *PASP*, 120, 328
- Maaskant, K. M., de Vries, B. L., Min, M., et al. 2014, arXiv:1406.3951
- Malfait, K., Waelkens, C., Waters, L. B. F. M., et al. 1998, *A&A*, 332, L25
- Marois, C., Macintosh, B., Barman, T., et al. 2008, *Science*, 322, 1348
- Marois, C., Zuckerman, B., Konopacky, Q. M., Macintosh, B., & Barman, T. 2010, *Nature*, 468, 1080
- Matthews, B., Kennedy, G., Sibthorpe, B., et al. 2014, *ApJ*, 780, 97
- Mayor, M., Marmier, M., Lovis, C., et al. 2011, arXiv:1109.2497
- Meshkat, T., Bailey, V., Rameau, J., et al. 2013, *ApJ*, 775, L40
- Meshkat, T., Bailey, V., Su, K. Y. L., Kenworthy, M. A. et al. 2014, *ApJ*, submitted
- Moór, A., Ábrahám, P., Kóspál, Á., et al. 2013, *ApJ*, 775, L51
- Moore, A., & Quillen, A. C. 2013, *MNRAS*, 430, 320
- Morales, F. Y., Rieke, G. H., Werner, M. W., et al. 2011, *ApJ*, 730, L29
- Morrison, S., & Malhotra, R., 2014 *ApJ*, in press
- Moya, A., Amado, P. J., Barrado, D., et al. 2010, *MNRAS*, 405, L81
- Nilsson, R., Liseau, R., Brandeker, A., et al. 2010, *A&A*, 518, A40
- Popesso, P., Magnelli, B., Buttiglione, S., et al. 2012, arXiv:1211.4257
- Rameau, J., Chauvin, G., Lagrange, A.-M., et al. 2013a, *ApJ*, 772, L15
- Rameau, J., Chauvin, G., Lagrange, A.-M., et al. 2013b, *ApJ*, 779, L26
- Rhee, J. H., Song, I., Zuckerman, B., & McElwain, M. 2007, *ApJ*, 660, 1556
- Rizzuto, A. C., Ireland, M. J., & Zucker, D. B. 2012, *MNRAS*, 421, L97
- Sódor, Á., Chené, A.-N., De Cat, P., et al. 2014, *A&A*, 568, A106
- Stapelfeldt, K. R., Holmes, E. K., Chen, C., et al. 2004, *ApJS*, 154, 458
- Sturm, B., Bouwman, J., Henning, T., et al. 2013, *A&A*, 553, A5
- Su, K. Y. L., Rieke, G. H., Misselt, K. A., et al. 2005, *ApJ*, 628, 487
- Su, K. Y. L., Rieke, G. H., Stapelfeldt, K. R., et al. 2009, *ApJ*, 705, 314
- Su, K. Y. L., Rieke, G. H., Malhotra, R., et al. 2013, *ApJ*, 763, 118
- Su, K. Y. L., & Rieke, G. H. 2014, *IAU Symposium*, 299, 318
- Suto, H., Sogawa, H., Tachibana, S., et al. 2006, *MNRAS*, 370, 1599
- Thebault, P., Kral, Q., & Augereau, J.-C. 2014, *A&A*, 561, A16
- de Vries, B. L., Acke, B., Blommaert, J. A. D. L., et al. 2012, *Nature*, 490, 74
- Wisdom, J. 1980, *AJ*, 85, 1122
- Wyatt, M. C. 2005, *A&A*, 433, 1007
- Wyatt, M. C., Clarke, C. J., & Booth, M. 2011, *Celestial Mechanics and Dynamical Astronomy*, 111, 1
- Voshchinnikov, N. V., Il'in, V. B., & Henning, T. 2005, *A&A*, 429, 371
- de Zeeuw, P. T., Hoogerwerf, R., de Bruijne, J. H. J., Brown, A. G. A., & Blaauw, A. 1999, *AJ*, 117, 354